A Novel Immune Checkpoint Siglec-15 Antibody Inhibits LUAD by Modulating mφ Polarization in TME

Xuejun xiao
Xinjiang Medical University
Yan Peng
Nanjing Medical University
Zheyue Wang
Nanjing Medical University
Louqian Zhang
Nanjing Drum Tower Hospital, the Affiliated Hospital of Nanjing University Medical School
tingting yang
Nanjing Medical University
Yangyang Sun
Nanjing Medical University
Yufeng Chen
Nanjing Medical University
Wenqing Zhang
Nanjing Medical University
Xinxia Chang
Nanjing Medical University
wen huang
Nanjing Medical University
Shuning Tian
Nanjing Medical University
Zhenqing Feng
Nanjing Medical University
Nabi Xinhua
Xinjiang Medical University
Qi Tang
Nanjing Medical University
Yuan Mao (ymaoent@njmu.edu.cn)
Nanjing Medical University

Research Article

Keywords: Lung adenocarcinoma, siglec-15, checkpoint inhibitor, macrophage, tumor microenvironment

Posted Date: February 23rd, 2022

DOI: https://doi.org/10.21203/rs.3.rs-1373618/v1

Abstract

Background

Siglec-15 (S15) is a type-I transmembrane protein and is considered a new candidate of immune checkpoint inhibitor for cancer immunotherapy.

Methods

In the present study, we first constructed and characterized a chimeric S15-specific monoclonal antibody (S15-4E6A). Then, the antitumor effectiveness and modulatory role of S15-4E6A in macrophages (mφs) were explored *in vitro* and *in vivo*. Finally, the underlying mechanism by which S15mAb inhibits LUAD was preliminarily explored.

Results

The results demonstrated the successful construction of S15-4E6A, and S15-4E6A exerted an efficacious tumor-inhibitory effect on LUAD cells and xenografts. S15-4E6A could promote M1-mφ polarization while inhibiting M2-mφ polarization, both *in vitro* and *in vivo*.

Conclusions

S15-based immunotherapy that functions by modulating mφ polarization may be a promising strategy for the treatment of S15-positive LUAD.

Introduction

Lung cancer (LC) is one of the most common cancers and the leading cause of malignancy-related death worldwide (1). In LC, non-small cell lung cancer (NSCLC) accounts for more than 85% of cases and mainly comprises lung adenocarcinoma (LUAD), lung squamous cell carcinoma (LUSC), and large cell carcinoma (2). LUAD represents the most common histological type of NSCLC and was well acknowledged as the highest heterogeneity and aggressiveness (3). During the past five years, accumulating evidence revealed the achievements of encouraging survival advantage with the application of immune checkpoint inhibitors (ICIs) in LUAD management (4, 5). The roles of PD-1/PD-L1 and CTLA-4-targeted immunotherapy have been thoroughly outlined, and these novel medications have revolutionarily redefined the treatment strategies for LUAD (6, 7). However, several issues need to be addressed. For one thing, the available ICI therapies work in only a fractional of LUAD patients, and drug-resistance is inevitable. For another, the incidence of immune-related adverse events (irAEs) is nearly 40% in real-world in China, and some adverse events are lethal (8, 9). Given the tremendous breakthrough in

anticancer treatment achieved with ICIs and the existing disadvantages of PD-1/PD-L1/CTLA-4-based ICIs in clinical application, it is of great necessity to develop novel types of ICIs.

Siglec-15 (S15) is a type-I transmembrane protein and consists of three parts that collectively contain 328 amino acids (aa): two immunoglobulin (Ig)-like domains, a transmembrane domain including a lysine residue, and a short cytoplasmic tail. The extracellular domain is comprised of an N-terminal sialic acid-binding V-set domain (IgV) and a C2-set domain (IgC2), in which the IgV is the dominant binding site in S15 for sialyl-Tn (sTn) (10, 11). S15 was originally characterized as a modulator of osteoclast differentiation and bone remodeling, and has recently attracted much attention because of its multiple roles in tumor immunology (12, 13). Dr. Lieping Chen, who first identified the PD-1/PD-L1 pathway in cancer immunotherapy, reported upregulation of S15 in tumor cells and tumor associated macrophages (TAMs), leading to profound immunosuppression in the tumor microenvironment (TME). He described S15 as a new candidate responsible for adaptive immune resistance and a potential target for normalization cancer immunotherapy. Notably, S15 expression is mutually exclusive with that of PD-L1, implying that anti-S15 therapy might extend therapeutic benefits to patients who do not respond to anti-PD-1/PD-L1 treatment (14–16). The relationships between S15 expression and the clinicopathological parameters of LUAD were elaborately investigated, by both bioinformatic analysis and evaluation of a private cohort (17). In detail, high expression of S15 could be detected in LUAD, and elevated S15 mRNA and protein expression significantly correlated with a poor prognosis in LUAD patients. In addition, S15 was positively associated with M0-macrophage (M0) expression in LUAD patients. The above distinctive molecular features of S15 highlight its therapeutic potential in LUAD management.

In the present study, we first constructed and characterized a chimeric S15-specific monoclonal antibody (S15mAb). Then, the antitumor effectiveness of S15mAb was investigated *in vitro* and *in vivo*. Finally, the underlying mechanism by which S15mAb inhibits LUAD was preliminarily explored.

Materials And Methods

Cell lines

The human glioblastoma cell line U87MG, human hepatocellular carcinoma cell line HepG2, human prostate cancer cell line PC-3, human monocytic leukemia cell line THP-1, human large cell lung carcinoma cell line H460 and human LUAD cell lines A549, H1299, H1975, and PC9 were purchased from the Cell Bank of the Chinese Academy of Sciences (Shanghai, China). Luciferase-labeled mouse Lewis lung carcinoma cells (LLC-luc) were customized by Meisen Cell Biotechnology Co., Ltd. (Hangzhou, China). A normal human bronchial epithelial (HBE) cell line and the 293T and 293F cell lines were preserved in our laboratory and enrolled in the present study. Specifically, an S15 knockdown model established in the A549 cell line (shS15) and an S15 overexpression model established in the HBE cell line (OES15) were prepared as previously described (18).

Reagents

A recombinant sTn protein was purchased from Sino Biological (Beijing, China). Human cytokine enzyme-linked immunosorbent assay (ELISA) detection kits were purchased from InvivoGen (CA, USA). Other information for important reagents is summarized in Supplementary Table S1. A goat anti-human IgG-Fc secondary antibody was purchased from Thermo Scientific (MA, USA). A polyclonal rabbit anti-human S15 antibody was purchased from LSBio (WA, USA). Other antibody information is summarized in Supplementary Table S2.

Database search and antigen determination

General information on S15 was retrieved from the SWISS-MODEL Repository (https://swissmodel.expasy.org). The subcellular location of S15 was investigated in the GeneCard database (http://www.genecards.org), and the UniProt database (https://www.prot.org) was searched to identify the detailed aa sequences of S15 and determine the overlapping peptide template. A recombinant S15 protein was designed and customized by Genscript Biotech Co., Ltd. (Nanjing, China). The S15 expression mode in various cell lines was determined from the Oncomine (https://www.oncomine.org/) and The Human Protein Atlas (https://www.proteinatlas.org/) databases.

Hybridoma preparation

Three 6- to 8-week-old BALB/c mice (SLAC Laboratory, Shanghai, China) were subcutaneously injected in the abdomen with 100 μg of recombinant S15 protein (the first, third, and fifth times) or ovalbumin (OVA)-conjugated mixed polypeptide (the second and fourth times) as the immunogen for immunization. After measuring the serum antibody titer by ELISA (19), the hyperimmunized mice were intravenously boosted with the OVA-conjugated mixed polypeptide three days before cell fusion. Then, splenocytes were isolated and fused with the SP2/0 murine myeloma cell line using 50% polyethylene glycol (PEG). The fused cells were cultured in hypoxanthine/aminopterin/thymidine (HAT, Sigma, USA) for 7 days.

Screening and identification of specific hybridoma clones

96-well ELISA microplates (Corning, NY, USA) were coated with 100 μl of 20 μg/ml recombinant S15 protein in coating buffer (0.1 M, pH 9.6) overnight at 4°C. After washing with phosphate-buffered saline (PBS) containing 0.05% Tween 20 (PBST) five times and blocking with 10% bovine serum albumin (BSA), the plates were incubated with 50 mL of hybridoma supernatants for 1 h at 37°C, followed by a 1-h incubation with horseradish peroxidase (HRP)-conjugated goat anti-mouse IgG (Thermo Fisher, MA, USA) at a 1:5000 dilution. After adding a peroxidase substrate chromogenic solution and 2 M sulfuric acid, the reaction was stopped, and optical densities (ODs) were measured. A positive hybridoma clone was identified by an OD value 2.5 times greater than the normal mouse serum OD value, and a candidate clone that could stably secrete mouse-S15mAb (mS15mAb) was selected. ELISA analysis was performed to detect the ability of mS15mAb to bind to an S15 antigen as previously described (20). An antibody subtype identification kit (ISO-2KT, Sigma, USA) was employed to detect the IgG-subtype of mS15mAb.

Chimeric antibody generation, purification and characterization

Total RNA extraction and cDNA reverse transcription were performed for selected hybridoma clones(21). The BLAST database (https://blast.ncbi.nlm.nih.gov/Blast.cgi) was consulted to design VH forward primers and Vλ forward primers. After mixing these primers, the cDNA of the selected clone was used as a template to amplify the antibody variable regions as previously described (19). The IgG expression plasmids pFUSE-CHIg-hG1, and pFUSE-CLIg-hl (InvivoGen) which contain IgG1 type human CH and Cλ sequences, were employed to perform infusion PCR and eukaryotic expression of chimeric S15mAb (22). Then, S15mAb in the culture supernatant was purified by affinity chromatography using Protein A (GE Healthcare, IL, USA) on an AKTA purifier 100 according to the manufacturer's protocols (23). ELISA analysis was performed as described above to detect the binding activity of S15mAb for S15 (20). Then, SDS-PAGE and Western-blotting (WB) were conducted to investigate the purity and specificity of S15mAb, followed by immunofluorescence (IF) analysis to detect the subcellular location of the S15 protein that S15mAb could recognize in positive S15-expressing LUAD cell line as previously described (20).

Epitope mapping detection and competitive binding assays

ELISA tests were performed to conduct epitope mapping detection and competitive binding assays. For epitope mapping detection, diverse sequences of antigenic S15 peptides were designed, prepared and diluted to 2 μg/mL for coating. S15mAb at various concentrations (starting at 2 μg/mL, four concentration gradient dilutions) was added. Discovery Studio 2019 software (Dassault Systèmes Biovia, CA, USA) was employed to visualize a 3D diagram of the recognition of S15 by S15mAb (24). The simulation model was operated to analyze the molecular interaction, and the charmm force field was implemented to calculate the binding force (25, 26). For the competitive binding assay, S15 protein at a fixed concentration (2 μg/mL) was used for coating. Then, gradient dilutions of S15mAb and a polyclonal S15-specific antibody (S15pAb) were added with fixed sTn protein (2 μg/mL). In particular, the locus at which S15pAb reacted with S15 was aa 274–302 (https://www.lsbio.com/). Three segments of synthesized S15 peptides were then screened to further validate the competitive binding of S15mAb with a particular section of the S15 peptides. The detailed protocols were described previously (20).

Phenotypic experiments with cancer cells

S15 expression in several human lung cancer cell lines and LLC-luc cell line was detected by WB analysis as previously described (27). For LUAD cell line, cell proliferation was firstly examined in A549 cell after administration of S15mAb with various concentration (5 μg/mL-80 μg/mL) to determine the optimal dosage. Then four LUAD cell lines (A549, H1299, H460, PC9) with differential S15 expression were enrolled to detect tumor-inhibitory effectiveness of S15- S15mAb by CCK-8 and transwell assays (28). HBE cell line was used as negative control. Cell proliferation, migration and apoptosis were examined by CCK-8, wound healing and flow cytometry (FCM) analyses (27, 29, 30).

Phenotypic experiments with macrophages (mφs)

For mφ experiments, we used phorbol 12-myristate-13-acetate (PMA) to induce the differentiation of THP-1 cells into mφs (31). Then, we employed lipopolysaccharide (LPS) and IL-4/IL13 separately to induce the

two major polarization states of mφs, the classically activated type 1 (M1-mφ) and alternatively activated type 2 (M2-mφ) phenotypes, respectively (32). S15mAb was then administered to two different mφ groups to explore its modulatory activities. CCK-8 assay was performed to investigate mφ proliferation and the M1/M2 mφ status, while WB and ELISA were performed to detect the expression of M1 and M2 mφ markers and related cytokines (21).

Orthotopic xenograft experiment

The animal studies were conducted in accordance with Public Health Service Policy and approved by the Animal Care and Use Committee of Nanjing Medical University. A total of 35 C57BL/6 mice were purchased from SLAC Laboratory Animal (Shanghai, China). The LLC-luc cell line was used to construct a LUAD orthotopic xenograft model. Specifically, a total of mice were injected with 1×10^6/mL LLC-luc cells with Matrigel (1:1 ratio by volume) in the lungs (33). After the inoculation, 28 tumor-bearing mice were divided randomly into 4 treatment groups, and each mouse was injected intravenously on days 0, 6, 12, and 18 with S15mAb at different concentrations: LUAD xenograft-bearing mice were treated with a low concentration (LL, 1 mg/kg), moderate concentration (LM, 5 mg/kg) or high concentration (LH, 10 mg/kg). LUAD xenograft-bearing mice treated with PBS were used as the control group (LC). In addition, 7 healthy C57BL/6 mice without LLC-luc cell inoculation treated with PBS were used as a negative control (NC). The orthotopic xenografts were monitored, measured and recorded with bioluminescence imaging by employing an IVIS Lumina II (PerkinElmer, Hopkinton, MA, USA) as previously described (21). On day 24, 28 tumor-bearing mice were sacrificed, and the xenograft tumors were removed for further analysis. Hematoxylin and eosin (H&E) staining and immunohistochemistry (IHC) analysis were performed, and the detailed protocols were described previously (34) .

Modulatory effectiveness of S15mAb in mice

To explore the gene expression profile induced in response to S15mAb in orthotopic xenografts in vivo, RNA sequencing (RNA-seq) was employed to screen differentially expressed genes (DEGs) after S15mAb administration to mice. Total RNA was extracted using TRIzol reagent, and RNA-seq was conducted as previously described (35). Briefly, after extracting RNA from xenograft tumors in the various S15mAb treatment groups, mRNA was enriched and reverse transcribed for RNA-seq. Gene annotation was performed with reference to the GRCh38 (hg38) genome, followed by gene expression analysis (36). A corrected P-value (padj) < 0.05 and log2FoldChange > 0 were selected as the thresholds for identifying significant DEGs between the S15mAb treatment and control groups. Gene Ontology (GO) and Kyoto Encyclopedia of Genes and Genomes (KEGG) pathway enrichment analyses of DEGs were implemented with clusterProfiler (37). The Cancer Genome Atlas (TCGA) database was consulted to investigate the differential expression and prognostic characteristics of related genes (21). qPCR, WB and IHC analyses were further performed to investigate and confirm the differential expression of mφ markers, mφ-related genes and signaling pathway markers as previously described (22, 28). Apoptotic gene expression was detected by WB as previously described (29). All primer sequences for qPCR are listed in Supplementary Table S3.

Statistical analysis

All data are shown as the means ± standard deviations (SD). Intergroups differences were analyzed by one-way ANOVA or Student's t-test with STATA 14.0 (Stata Corporation, College Station, TX, USA) or SPSS 18.0 (SPSS Inc, Chicago, IL, USA). The significance level was set at $p < 0.05$.

Results

Bioinformatic analyses and S15 antigen preparation

S15 comprises a total of 328 aa, and the overall structure of the S15 protein is shown in Supplementary Figure S1A (https://swissmodel.expasy.org/). The subcellular location of S15 is shown in Supplementary Figure S1B (http://www.genecards.org). The detailed structure of the extracellular domain of S15 contains an IgV (aa 40–158) and IgC2 (aa 168–251), and aa 143 was the principal binding site in S15 for sTn, which is demonstrated in Supplementary Figure S1C (https://www.uniprot.org). We employed aa 37–180 of the extracellular domain of S15 as a template and designed overlapping peptides, which were termed A1-A12 and B1-B11 (Table 1). After the peptides were synthesized, mixed and coupled with OVA and hemocyanin (KLH), respectively, the recombinant S15 antigen was successfully prepared. In addition, U87MG, PC-3 and A549 cells were positive for S15 expression (https://www.proteinatlas.org, https://www.oncomine.org). THP-1 cells exhibited low S15 expression [18]. HepG2 cells were negative for S15 expression (https://www.proteinatlas.org) (Supplementary Figure S1D and S1E).

Construction, expression and purification of S15mAb

Culture supernatants from hybridoma cells were screened before and after cloning and subcloning using a recombinant S15 protein. A single hybridoma clone that could stably secrete an antibody was identified and named mouse-4E6A (m4E6A); this clone was further used for total RNA extraction and cDNA reverse transcription. ELISA analysis proved that the m4E6A antibody could recognize the S15 protein properly (Supplementary Figure S2A). Isotype analysis further showed that the subtype of the m4E6A antibody was IgG1. Then, VH and Vλ from the m4E6A clone were amplified and separately cloned into two eukaryotic expression vectors (pFUSE-CHIg-hG1 and pFUSE-CLIg-hl) by IF-PCR (Supplementary Figure S2B and S2C). The two recombinant expression vectors were cotransfected into FreeStyle™ 293 cells, and the cell supernatant was harvested after 5 days of culture for subsequent purification to prepare the novel recombinant human-mouse chimeric antibody S15mAb (S15-4E6A).

Characterization of S15-4E6A

SDS-PAGE was performed, and the data shown in Fig. 1A validated the successful construction of S15-4E6A. ELISA was performed to test the binding sensitivity of S15-4E6A for the S15 protein. As shown in Fig. 1B, S15-4E6A recognized the S15 protein in a dose-dependent manner. WB demonstrated that S15-4E6A could react with S15-positive cell lines, including U87MG, PC-3, THP-1, and A549 cells, but rarely recognized the S15-negative cell line HepG2 (Fig. 1C). A BLITz affinity assay suggested that the

equilibrium dissociation constant (Kd) for S15-4E6A was 5.719×10^{-8} M (Fig. 1D). IF analysis further proved that S15 could be stained by S15-4E6A in the A549 (S15-positive) cell line. In the shS15 group, in which S15 was downregulated, the staining intensity of S15-4E6A was significantly decreased. The U87MG cell line was employed as a positive control. Strong staining of S15 was mainly localized in the cytomembrane, while relatively weak staining of S15 was observed in the cytoplasm of cancer cells (Fig. 1E).

S15-4E6A competitively inhibits the binding of sTn to S15

An epitope mapping test showed that the OD value of the A9 segment (aa 133–144) was the highest among the segment OD values when the polypeptide dilution ratio was 1:100, indicating that the A9 sequence included the principal binding site in S15 for S15-4E6A (Fig. 2A, 2B and 2C). Figure 2D depicts the 3D diagram of the recognition locus in S15-4E6A for S15. The blue segment indicates the S15 protein, while the khaki portion represents S15-4E6A. The red section indicates the binding site locus at aa 143. The results of a competitive inhibition test demonstrated that S15-4E6A could increasingly bind to S15 in a dose-dependent manner, which progressively weakened the binding of sTn to S15. In comparison, S15pAb rarely changed the binding of sTn to S15 (Fig. 2E). Moreover, Fig. 2F further confirms the positive binding ability of three epitope sites (A9, B8 and B9) in S15-4E6A, among which the A9 sequence demonstrated the most significant binding ability.

S15-4E6A inhibits LUAD malignant behaviors *in vitro*

Figure 3A illustrates S15 expression in several human lung cancer cell lines and LLC-luc cell line. The A549 cell line was then employed, and S15-4E6A was administered at different concentrations (5 μ/mL-80 μg/mL) to determine the optimal S15-4E6A dose. A dose-effect curve was first drawn, and the 50% inhibitory concentration (IC50) of S15-4E6A in A549 cells was 1.505. The appropriate concentration of 20 μg/mL S15-4E6A was selected for further experiments (Fig. 3B). A CCK-8 assay was then performed to investigate the role of S15-4E6A in various LUAD cell lines. The results showed that the inhibition efficiency of S15-4E6A significantly increased in a time-dependent manner in S15-positive cells but not in S15-negative cells (Fig. 3C). Transwell analysis revealed that the number of invasive cells with high S15 expression was significantly lower than that of cells with low S15 expression after treatment with S15-4E6A (Fig. 3D). After successfully constructing shS15 and OES15 models (Supplementary Figure S3A, S3B and S3C), CCK-8 (Fig. 4A), wound healing (Fig. 4B) and Annexin V/propidium iodide (PI) assays (Fig. 4C) demonstrated that cell proliferation and migration were dramatically increased, while apoptosis was significantly decreased when S15 expression was knocked down in the A549 cell line after S15-4E6A administration. In comparison, cell proliferation and migration were critically suspended, while apoptosis was dramatically augmented when S15 was overexpressed in an HBE cell line.

S15-4E6A modulates mφ characteristics *in vitro*

After induction by PMA followed by LPS or IL-4/IL13 treatment, S15-4E6A was administered to two different mφ groups (Fig. 5A). Compared with PBS, S15-4E6A dramatically boosted the cell proliferation

rate in the M1-mφ induction group but inhibited the cell proliferation rate in the M2-mφ induction group (Fig. 5B). WB showed that the M1-mφ marker (iNOS) and related genes (HLA-DR and TNF-α) were upregulated, while the M2-mφ marker (Arg-1) and related genes (VEGF and CCL22) were downregulated after S15-4E6A administration in the M1-mφ and M2-mφ induction groups (Fig. 5C). ELISA also showed that antitumor cytokines were elevated (TNF-α and IL-6), while protumor cytokines (TGF-β and IL-10) were downregulated after S15-4E6A was administered in both the M1 and M2-mφ groups (Fig. 5D).

S15-4E6A inhibits LUAD orthotopic xenograft *in vivo*

LUAD orthotopic xenograft models produced by inoculation of C57BL/6 mice with LLC-LUC cells were constructed to explore the antitumor effectiveness of S15-4E6A, following the protocol shown in Fig. 6A. Bioluminescence imaging of LUAD xenografts derived from luciferase-expressing LLC-LUC cells demonstrated a dramatic effect on tumor inhibition upon S15-4E6A administration, and the LH group illustrated the most significant tumor-inhibitory effectiveness (Fig. 6B and 6C). On day 24, all mice were sacrificed, and the xenograft tumors were removed and analyzed. Tumor morphology and weight results further illustrated that S15-4E6A could specifically target and significantly restrain S15-positive LUAD orthotopic xenograft tumor growth in vivo (Fig. 6D). H&E staining confirmed that necrotic areas and interstitial fibrosis were present after high-dose S15-4E6A administration (Fig. 6E). IHC analysis further proved that as the S15-4E6A concentration increased, TTF expression gradually decreased (Fig. 6F). Moreover, organ functions, as indicated by alanine transaminase (ALT), aspartate transaminase (AST), creatinine (CREA), and carbamide (UREA), were monitored, and no abnormal liver or renal function was observed after S15-4E6A administration (Supplementary Figure S4A). The thymus and spleen coefficients of mice were rarely changed after S15-4E6A treatment (Supplementary Figure S4B).

RNA-seq analysis and bioinformatics consultant

RNA-seq analysis was conducted by Singleron Biotechnologies (Nanjing, China). The normalized expression level of each gene was measured and corrected by the expected number of Fragments Per Kilobase of transcript sequence per Million base pairs sequenced (FPKM). We clustered the identified DEGs to investigate the mode of expression of different genes under various S15-4E6A concentrations. The top 50 most significantly upregulated genes are shown in Fig. 7A. We found that the upregulated GO terms included second-messenger-mediated signaling, cell-cell junction, receptor complex, and cell adhesion molecule binding (Fig. 7B). KEGG enrichment results showed that the DEGs were significantly enriched in cell adhesion molecules, the cAMP signaling pathway, ECM-receptor interaction, and cGMP-PKG signaling pathways (Fig. 7C). We consulted the TCGA database and identified 6 genes (RHBDL2, CELF5, PLAC1, EGLN3, CCL7, and PVT1) with elevated expression (Fig. 7D) and 3 with potential prognostic characteristics (SHOX2, CD109, and PRSS22) in LUAD (Fig. 7E). Then, we further clustered the mφ-related DEGs, and the expression of typical selected genes associated with M1 mφs (CCL6, CCL8, CD86, CXCL2, CXCL9, CXCL10, IL6, and TNFAIP3) or M2 mφs (CD68, CD163, CXCR4, IL4, MRC1, NOS1, PIGF, and VEGFD) in different treatment groups is illustrated in Fig. 7F and 7G.

DEG and mφ-polarization in S15-4E6A-treated mice

A number of DEGs associated with mφ polarization or the siglec family were identified in in vivo experiments and validated by qPCR and WB. As shown in Fig. 8A and 8B, S15-4E6A treatment significantly inhibited the expression of DAP12, SYK, p-SYK, and NF-κB. IHC analysis proved that the expression of CD68 and CD163 was dramatically downregulated in the LH S15-4E6A group, with the $CD68^{+}CD163^{+}$ phenotype being a typical biomarker of M2-mφs (Fig. 8C). Similarly, qPCR and WB results further demonstrated that M1 mφ-related markers (iNOS, HLA-DR, and TNF-α) were upregulated (Fig. 8D and 8E), while M2 mφ-related markers (Arg-1, VEGF, CCL22) were downregulated in mice after S15-4E6A administration (Fig. 8F and 8G). Apoptotic factor results also revealed that antiapoptotic factors such as Bcl-2 were significantly downregulated, while proapoptotic factors including Bax and caspase-3 were dramatically upregulated in the S15-4E6A LH group compared with the control group (Fig. 8H and 8I).

Discussion

Current PD-1/PD-L1/CTLA-4-targeted immunotherapies have led to remarkable response rates and survival benefits in a subset of LUAD patients. However, the available therapies work in only approximately 20% of unselected, advanced NSCLC patients, and primary and acquired resistance are still unresolved impediments (38, 39). Recent studies have identified S15 as an important immunosuppressor in the TME, and S15 could be theoretically identified as a complementary target for LUAD immunotherapies targeting PD-1/PD-L1/CTLA-4 (14, 40). Although an anti-S15 antibody, NC318, has been administered in several clinical trials on NSCLC, exploration of novel anti-S15 regimens should not be suspended (41, 42).

In the present study, we first designed an S15 protein as the original antigen based on its structure and characteristics. After constructing the recombinant S15 whole-gene protein, we employed hybridoma technology to screen m4E6A. The human eukaryotic expression vectors pFUSE-CHIg-hG and pFUSE-CLIg-hl were used to replace the primitive CH and Cλ sequences of mouse IgG. Recombinant expression vectors were then produced by IF-PCR. After transfection and purification, we successfully produced the novel anti-S15 chimeric antibody S15-4E6A. SDS-PAGE and WB confirmed the purity and specificity of S15-4E6A, which showed a specific binding capacity for an S15 antigen by ELISA and a BLITz affinity assay. Moreover, our IF assay illustrated that S15 could be recognized by S15-4E6A and that the subcellular location of S15 was mainly in the cytomembrane of a LUAD cell line. Li et al. also noted membrane staining of S15 in LUAD tissue samples (17).

As Angata et al. previously reported that aa 143 is the dominant recognition locus for sTn in S15 (12), we elaborately designed 23 peptide segments to investigate the binding locus for S15-4E6A in S15. The results of the epitope mapping test showed that the OD value of the A9 segment (aa 133–144), which included the locus aa 143, was the highest. Then, S15pAb, which exhibited very low recognition of the locus aa 143, was evaluated in the competitive binding assay, and the data further confirmed that compared with sTn, S15-4E6A could competitively bind to the S15 protein.

The antitumor activity of S15-4E6A was then explored in a LUAD cell line *in vitro*. The CCK-8 assay results showed that the inhibitory efficiency of S15-4E6A increased in a time-dependent manner, and the difference was statistically significant. Transwell assay results demonstrated that S15-4E6A could inhibit tumor cell migration by various types of S15-positive LUAD cell lines compared to cells without S15 expression. Then, we constructed shS15 and OES15 models to validate the tumor-inhibitory effectiveness of S15-4E6A. The results of CCK-8 and wound healing assays proved the substantial cytotoxicity of S15-4E6A to a LUAD cell line. Annexin V/PI assays further revealed that S15-4E6A performed a proapoptotic role in S15-positive cell lines. Although an anti-S15 monoclonal antibody (α-S15) achieved encouraging results in xenograft models and NC318 has been administered in a clinical trial (41, 43), our present information provides detailed characteristics and complementary data for LUAD treatment with S15-4E6A *in vitro*.

S15 is a mφ-associated T cell-immunosuppressive molecule, and it was reported that α-S15 suppresses osteoclast differentiation in the RAW264.7 mouse mφ cell line (44). However, this previous study failed to distinguish the classification of mφs after using α-S15. In this study, we first investigated the influence of S15-4E6A on M1/M2 mφ proliferation. After LPS (M1-mφ induction) or IL4/IL13 (M2-mφ induction) administration, S15-4E6A tended to induce the proliferation of M1-mφs but inhibit the proliferation of M2-mφs. In other words, S15-4E6A exhibited stronger inhibitory effectiveness against M2 mφs than against M1 mφs, which was further proven by the differential expression of M1/M2 mφ-related markers. Moreover, we detected the expression of selected cytokines, and the results showed that antitumor cytokines (TNF-α and IL-6) were elevated, while protumor cytokines (TGF-β and IL-10) were decreased after S15-4E6A treatment. The data largely agreed with the results of a number of previous studies. For example, Takamiya et al. observed upregulation of S15 in M2 mφs, and S15 could promote tumor metastasis and induce tumor immunosuppression by enhancing TGF-β production (45). Miguel et al. showed that S15 could inhibit T cell activity in an IL-10-dependent manner (46). Nejad et al. reported that IL-6 signaling was critical during the process of immunotherapy-driven tumor regression (47). The above information implied that S15-4E6A could exert diverse regulatory functions in mφs in different polarization states and thus affect the immunological status of the TME.

An orthotopic xenograft tumor model was constructed, and an *in vivo* experiment thoroughly proved the tumor-inhibitory competence of S15-4E6A. The tumor burdens of mice were much lower in the S15-4E6A treatment groups than in the control group, and better survival outcomes were observed for mice in the LH S15-4E6A group than for those in the control group. No severe organ function failures were witnessed after S15-4E6A administration in mice, suggesting that the adverse effects of S15-4E6A were tolerable. As mentioned above, Wang et al. also reported that anti-S15 monoclonal antibodies (mAbs) blocked inhibitory effects on T cell activities and suppressed the growth of established tumors in mice (13).

As the TME is a highly complicated, heterogeneous and evolving ecosystem, the relationship between S15 and mφs in the TME may be relatively complex. Our RNA-seq data for orthotopic xenografts first defined the top 50 DEGs and identified 9 genes with differential expression and prognostic potential. Then, we focused on the mφ-related DEGs and listed selected genes associated with M1 or M2 mφs. Our

present data are supported by the findings of a series of previous studies. For instance, Yang et al. reported that PLAC1 was upregulated in NSCLC tissues and that this high expression was associated with an advanced pathological stage and shorter progression-free survival (PFS) (48). Han et al. found that high CCL7 expression was associated with migration, invasion and bone metastasis of NSCLC (49). Li et al. noted that SHOX2 was highly expressed in LUAD and that high SHOX2 expression or hypomethylation indicated poor differentiation and a poor prognosis (50). For mφ-related DEGs, recent findings emphasize that M1 mφs, M2 mφs and any intermediate states are not fixed, frozen or immutable but remarkably plastic and transmutative (51), so the characteristics of certain mφ-associated genes have been found to be diverse, indeterminate or even paradoxical. For example, Ji et al. reported that CCL8 could enhance the sensitivity of cutaneous squamous cell carcinoma to photodynamic therapy by recruiting M1 mφs, suggesting an antitumor role for CCL8 (52). In contrast, Zhang et al. found that CCL8 secreted by TAMs could promote the invasion and stemness of glioblastoma via ERK1/2 signaling, which implied a protumor function for CCL8 (53). However, we also identified positive expression of selected M2 mφ-associated genes with acknowledged oncogenic behaviors, such as CXCR4. Selective antagonists of CXCR4, the receptor of CXCL12, have been successfully developed, and the CXCL12-CXCR4 interaction has emerged as a promising target for immunotherapy to be tested in clinical trials (54–56).

Interestingly, previous cancer immunotherapy efforts focused more attention on amplifying antitumor immunity above physiological levels, which produced limited clinical responses and off-tumor toxicities (16). Chen et al. highlighted that it might be more important to restore the equilibration of immune function in the TME, rather than consistently enhance immunity, so that the immune system could be maintained at the appropriate intensity to maintain the balance in the body while killing the tumor (46, 57, 58). In the present study, we enrolled healthy C57BL/6 mice without LLC-luc cell inoculation treated with PBS as a control group to simulate the normal immune system for further investigation of the modulatory effectiveness of S15-4E6A in the TME *in vivo*. The DAP12 gene is a transmembrane receptor that is widely expressed on the surface of natural killer cells, granulocytes, and macrophages. S15 can interact with and stabilize DAP12 in M2 TAMs and activate SYK and NF-κB signaling to promote tumor metastasis (59). After S15-4E6A treatment, we observed that DAP12, SYK, p-SYK, NF-κB in LH group were significantly down-regulated compared with that of in LC group, while were barely changed compared with that of in NC group. As S15-4E6A could competitively bind to S15 protein compared with that of sTn, the current information highly implied that DAP12-SYK-NF-κB signaling may be involved in S15-4E6A modulatory activity. The subsequent detection of M1/M2-mφ markers and related genes by IHC staining, qPCR and WB also confirmed these findings that the administration of S15-4E6A could suspend M2-mφ development and induce apoptosis. Our data that S15-4E6A adjusted the M1/M2-mφ expression in mice were in accordance with the novel and updated concept of immunological normalization in cancer immunotherapy that proposed by Dr. Chen (14). Future studies with large sample sizes are necessary to validate our present outcomes.

There are several issues related to the present study. In particular, Chen et al. noted that S15 potentially serves as a complementary therapeutic target and that targeting S15 may become a powerful supplementary approach for PD-1/PD-L1 inhibitors. Moreover, anti-S15 antibodies combined with anti-

PD-1/PD-L1 antibodies might produce a synergistic effect (14, 43). In the present study, we focused on only S15 expression and did not explore the relationship between S15 expression and PD-L1 expression in LUAD. We administered only a single agent, S15-4E6A, in *in vitro* and *in vivo* experiments and did not employ combination immunotherapy. In addition, Gavuthami et al. reported that S15 rarely recognized sTn while bound to sialylated glycans in a lung cancer cell line (60). In the present study, we observed that S15-4E6A could competitively inhibit the binding of S15 to sTn, which was inconsistent with the report by Gavuthami et al. Above all, the mechanism by which S15-4E6A exerts effects on LUAD was not fully elucidated by the present study. How S15-4E6A modulates oncogenic cross-talk and interactions among different types of cells in the TME, such as cancer cells, TAMs, endothelial cells, and fibroblasts, is largely unknown. In fact, our research group is continuing to ameliorate therapeutic effectiveness and further investigate the mechanism of S15-4E6A in LUAD. The strategies include the design of an S15/PD-1 dual-targeting antibody to produce a synergistic effect and improve tumor antigen recognition, the utilization of single-cell RNA sequencing (scRNA-seq) to characterize individual cellular interactions at the single-cell level in the TME, and the employment of multicolor immunocytochemistry/IF to describe the spatial connections of diverse proteins in various types of cells.

Conclusions

In conclusion, our present study demonstrated that targeting S15 is a prospective strategy for LUAD management. The novel antibody S15-4E6A exerts notable antitumor activity against S15-positive LUAD by modulating the polarization of mφs. This research provides promising insight and direction for LUAD immunotherapy.

Abbreviations

S15
Siglec-15
LUAD
lung adenocarcinoma
NSCLC
non-small cell lung cancer
ICIs
immune checkpoint inhibitors
irAEs
immune-related adverse events
Ig
immunoglobulin
sTn
sialyl-Tn
TAMs

tumor associated macrophages
TME
tumor microenvironment
LLC-luc
Luciferase-labeled mouse Lewis lung carcinoma cells
HBE
human bronchial epithelial
ELISA
enzyme-linked immunosorbent assay
PEG
polyethylene glycol
HAT
hypoxanthine/aminopterin/thymidine
PBS
phosphate-buffered saline
BSA
bovine serum albumin
HRP
horseradish peroxidase
ODs
optical densities
WB
Western-blotting
FCM
flow cytometry
mφs
macrophages
PMA
phorbol 12-myristate-13-acetate
LPS
lipopolysaccharide
H&E
hematoxylin and eosin
IHC
immunohistochemistry
TCGA
The Cancer Genome Atlas.

Declarations

Acknowledgements

None.

Funding

This work is supported by the grants from the National Natural Science Foundation (no. 81773100 to Zhenqing Feng; no. 81773268 to Qi Tang; no. 82073389 to Yuan Mao), the Young Scientist Project of Jiangsu Provincial Commission of Health and Family Planning (no. QNRC2016535 to Yuan Mao), the Natural Science Foundation of Jiangsu Province (BK20181489 to Yuan Mao), the Six Talent Peaks Project of Jiangsu Province (2015-WSN-017 to Yuan Mao), the National Natural Science Foundation for Youth of China (no.81301951 to Yuan Mao).

Consent for publication

Not applicable.

Availability of data and materials

All data generated or analyzed during this study are included in the manuscript and its supplementary information files.

Author's contributions

NX, QT and YM designed the study. XX, YP, and ZW collected the cell lines. XX, LZ, YF, TTY, and WH collected and summarized reagent information. YS and YC performed the IHC analysis. XX, YP, WZ and XC performed in vitro and in vivo experiments. XX, TTY, WH and ST performed the statistics. YM and XX drafted the manuscript. ZF and NX polished the manuscript. NX, QT and YM supervised the study. All authors read and approved the final manuscript.

Ethical approval

All animal experiments were approved by the Animal Care and Welfare Committee of Nanjing Medical University (IACUC-2103049, IACUC-1804017).

Competing interests

The authors declare no competing interests.

References

1. Siegel RL, Miller KD, Fuchs HE, Jemal A. Cancer Statistics, 2021. CA Cancer J Clin. 2021;71(1):7–33.
2. Wang S, Tong X, Li C, Jin E, Su Z, Sun Z, et al. Quaking 5 suppresses TGF-beta-induced EMT and cell invasion in lung adenocarcinoma. EMBO reports. 2021:e52079.

3. Tavernari D, Battistello E, Dheilly E, Petruzzella AS, Mina M, Sordet-Dessimoz J, et al. Non-genetic evolution drives lung adenocarcinoma spatial heterogeneity and progression. Cancer Discov. 2021.
4. Mok TSK, Wu YL, Kudaba I, Kowalski DM, Cho BC, Turna HZ, et al. Pembrolizumab versus chemotherapy for previously untreated, PD-L1-expressing, locally advanced or metastatic non-small-cell lung cancer (KEYNOTE-042): a randomised, open-label, controlled, phase 3 trial. Lancet. 2019;393(10183):1819–30.
5. Nosaki K, Saka H, Hosomi Y, Baas P, de Castro G, Jr., Reck M, et al. Safety and efficacy of pembrolizumab monotherapy in elderly patients with PD-L1-positive advanced non-small-cell lung cancer: Pooled analysis from the KEYNOTE-010, KEYNOTE-024, and KEYNOTE-042 studies. Lung cancer. 2019;135:188–95.
6. Glode AE, May MB. Immune checkpoint inhibitors: Significant advancements in non-small cell lung cancer treatment. American journal of health-system pharmacy: AJHP : official journal of the American Society of Health-System Pharmacists. 2021.
7. Perets R, Bar J, Rasco DW, Ahn MJ, Yoh K, Kim DW, et al. Safety and efficacy of quavonlimab, a novel anti-CTLA-4 antibody (MK-1308), in combination with pembrolizumab in first-line advanced non-small-cell lung cancer. Annals of oncology: official journal of the European Society for Medical Oncology. 2021;32(3):395–403.
8. Uruga H, Mino-Kenudson M. Predictive biomarkers for response to immune checkpoint inhibitors in lung cancer: PD-L1 and beyond. Virchows Archiv: an international journal of pathology. 2021;478(1):31–44.
9. Chen X, Nie J, Dai L, Hu W, Zhang J, Han J, et al. Immune-Related Adverse Events and Their Association With the Effectiveness of PD-1/PD-L1 Inhibitors in Non-Small Cell Lung Cancer: A Real-World Study From China. Frontiers in oncology. 2021;11:607531.
10. Crocker PR, Paulson JC, Varki A. Siglecs and their roles in the immune system. Nature reviews Immunology. 2007;7(4):255–66.
11. Crocker PR, Redelinghuys P. Siglecs as positive and negative regulators of the immune system. Biochemical Society transactions. 2008;36(Pt 6):1467–71.
12. Angata T, Tabuchi Y, Nakamura K, Nakamura M. Siglec-15: an immune system Siglec conserved throughout vertebrate evolution. Glycobiology. 2007;17(8):838–46.
13. Cao G, Xiao Z, Yin Z. Normalization cancer immunotherapy: blocking Siglec-15! Signal transduction and targeted therapy. 2019;4:10.
14. Wang J, Sun J, Liu LN, Flies DB, Nie X, Toki M, et al. Siglec-15 as an immune suppressor and potential target for normalization cancer immunotherapy. Nature medicine. 2019;25(4):656–66.
15. Sun J, Lu Q, Sanmanmed MF, Wang J. Siglec-15 as an Emerging Target for Next-generation Cancer Immunotherapy. Clin Cancer Res. 2021;27(3):680–8.
16. Pan C, Liu H, Robins E, Song W, Liu D, Li Z, et al. Next-generation immuno-oncology agents: current momentum shifts in cancer immunotherapy. Journal of hematology & oncology. 2020;13(1):29.

17. Li B, Zhang B, Wang X, Zeng Z, Huang Z, Zhang L, et al. Expression signature, prognosis value, and immune characteristics of Siglec-15 identified by pan-cancer analysis. Oncoimmunology. 2020;9(1):1807291.
18. Zhang L, Mao Y, Mao Q, Fan W, Xu L, Chen Y, et al. FLOT1 promotes tumor development, induces epithelial-mesenchymal transition, and modulates the cell cycle by regulating the Erk/Akt signaling pathway in lung adenocarcinoma. Thoracic cancer. 2019;10(4):909–17.
19. Liu J, Yang D, Yin Z, Gao M, Tong H, Su Y, et al. A novel human monoclonal Trop2-IgG antibody inhibits ovarian cancer growth in vitro and in vivo. Biochemical and biophysical research communications. 2019;512(2):276–82.
20. Xiong S, Tang Q, Liang X, Zhou T, Yang J, Liu P, et al. A Novel Chimeric Anti-PA Neutralizing Antibody for Postexposure Prophylaxis and Treatment of Anthrax. Sci Rep. 2015;5:11776.
21. Mao Y, Fan W, Hu H, Zhang L, Michel J, Wu Y, et al. MAGE-A1 in lung adenocarcinoma as a promising target of chimeric antigen receptor T cells. Journal of hematology & oncology. 2019;12(1):106.
22. Mao Y, Wang J, Zhang M, Fan W, Tang Q, Xiong S, et al. A neutralized human LMP1-IgG inhibits ENKTL growth by suppressing the JAK3/STAT3 signaling pathway. Oncotarget. 2017;8(7):10954–65.
23. Yin Z, Mao Y, Zhang N, Su Y, Zhu J, Tong H, et al. A fully chimeric IgG antibody for ROR1 suppresses ovarian cancer growth in vitro and in vivo. Biomedicine & pharmacotherapy = Biomedecine & pharmacotherapie. 2019;119:109420.
24. Gogoi B, Chowdhury P, Goswami N, Gogoi N, Naiya T, Chetia P, et al. Identification of potential plant-based inhibitor against viral proteases of SARS-CoV-2 through molecular docking, MM-PBSA binding energy calculations and molecular dynamics simulation. Molecular diversity. 2021.
25. Lin F, Xiong M, Hao W, Song Y, Liu R, Yang Y, et al. A Novel Blockade CD47 Antibody With Therapeutic Potential for Cancer. Frontiers in oncology. 2020;10:615534.
26. Biswas R, Bagchi A. Inhibition of TRAF6-Ubc13 interaction in NFkB inflammatory pathway by analyzing the hotspot amino acid residues and protein-protein interactions using molecular docking simulations. Computational biology and chemistry. 2017;70:116–24.
27. Gu X, Mao Y, Shi C, Ye W, Hou N, Xu L, et al. MAGEC2 Correlates With Unfavorable Prognosis And Promotes Tumor Development In HCC Via Epithelial-Mesenchymal Transition. OncoTargets and therapy. 2019;12:7843–55.
28. Mao Y, Xu L, Wang J, Zhang L, Hou N, Xu J, et al. ROR1 associates unfavorable prognosis and promotes lymphoma growth in DLBCL by affecting PI3K/Akt/mTOR signaling pathway. BioFactors. 2019;45(3):416–26.
29. Tang X, Tang Q, Mao Y, Huang X, Jia L, Zhu J, et al. CD137 Co-Stimulation Improves The Antitumor Effect Of LMP1-Specific Chimeric Antigen Receptor T Cells In Vitro And In Vivo. OncoTargets and therapy. 2019;12:9341–50.
30. Mao Y, Zhang DW, Wen J, Cao Q, Chen RJ, Zhu J, et al. A novel LMP1 antibody synergizes with mitomycin C to inhibit nasopharyngeal carcinoma growth in vivo through inducing apoptosis and

downregulating vascular endothelial growth factor. International journal of molecular sciences. 2012;13(2):2208–18.

31. Starr T, Bauler TJ, Malik-Kale P, Steele-Mortimer O. The phorbol 12-myristate-13-acetate differentiation protocol is critical to the interaction of THP-1 macrophages with Salmonella Typhimurium. PLoS One. 2018;13(3):e0193601.
32. Genin M, Clement F, Fattaccioli A, Raes M, Michiels C. M1 and M2 macrophages derived from THP-1 cells differentially modulate the response of cancer cells to etoposide. BMC cancer. 2015;15:577.
33. Shen M, Xu Z, Xu W, Jiang K, Zhang F, Ding Q, et al. Inhibition of ATM reverses EMT and decreases metastatic potential of cisplatin-resistant lung cancer cells through JAK/STAT3/PD-L1 pathway. Journal of experimental & clinical cancer research: CR. 2019;38(1):149.
34. Ma Y, Zhang M, Wang J, Huang X, Kuai X, Zhu X, et al. High-Affinity Human Anti-c-Met IgG Conjugated to Oxaliplatin as Targeted Chemotherapy for Hepatocellular Carcinoma. Frontiers in oncology. 2019;9:717.
35. Mao Y, Zhang DW, Lin H, Xiong L, Liu Y, Li QD, et al. Alpha B-crystallin is a new prognostic marker for laryngeal squamous cell carcinoma. Journal of experimental & clinical cancer research: CR. 2012;31:101.
36. Yu M, Ren L, Liang F, Zhang Y, Jiang L, Ma W, et al. Effect of epiberberine from Coptis chinensis Franch on inhibition of tumor growth in MKN-45 xenograft mice. Phytomedicine: international journal of phytotherapy and phytopharmacology. 2020;76:153216.
37. Campbell KM, Lin T, Zolkind P, Barnell EK, Skidmore ZL, Winkler AE, et al. Oral Cavity Squamous Cell Carcinoma Xenografts Retain Complex Genotypes and Intertumor Molecular Heterogeneity. Cell reports. 2018;24(8):2167–78.
38. Chae YK, Arya A, Iams W, Cruz MR, Chandra S, Choi J, et al. Current landscape and future of dual anti-CTLA4 and PD-1/PD-L1 blockade immunotherapy in cancer; lessons learned from clinical trials with melanoma and non-small cell lung cancer (NSCLC). J Immunother Cancer. 2018;6(1):39.
39. Arora S, Velichinskii R, Lesh RW, Ali U, Kubiak M, Bansal P, et al. Existing and Emerging Biomarkers for Immune Checkpoint Immunotherapy in Solid Tumors. Advances in therapy. 2019;36(10):2638–78.
40. Zhu Z, Zhu J, Zhao J, Zhu K, Xu Q, Chen H. Natural receptor-based competitive immunoelectrochemical assay for ultra-sensitive detection of Siglec 15. Biosensors & bioelectronics. 2020;151:111950.
41. Attili I, Tarantino P, Passaro A, Stati V, Curigliano G, de Marinis F. Strategies to overcome resistance to immune checkpoint blockade in lung cancer. Lung cancer. 2021;154:151–60.
42. Angata T. Siglec-15: a potential regulator of osteoporosis, cancer, and infectious diseases. Journal of biomedical science. 2020;27(1):10.
43. Ren X. Immunosuppressive checkpoint Siglec-15: a vital new piece of the cancer immunotherapy jigsaw puzzle. Cancer biology & medicine. 2019;16(2):205–10.

44. Stuible M, Moraitis A, Fortin A, Saragosa S, Kalbakji A, Filion M, et al. Mechanism and function of monoclonal antibodies targeting siglec-15 for therapeutic inhibition of osteoclastic bone resorption. The Journal of biological chemistry. 2014;289(10):6498–512.
45. Takamiya R, Ohtsubo K, Takamatsu S, Taniguchi N, Angata T. The interaction between Siglec-15 and tumor-associated sialyl-Tn antigen enhances TGF-beta secretion from monocytes/macrophages through the DAP12-Syk pathway. Glycobiology. 2013;23(2):178–87.
46. Sanmamed MF, Chen L. A Paradigm Shift in Cancer Immunotherapy: From Enhancement to Normalization. Cell. 2018;175(2):313–26.
47. Beyranvand Nejad E, Labrie C, van Elsas MJ, Kleinovink JW, Mittrucker HW, Franken K, et al. IL-6 signaling in macrophages is required for immunotherapy-driven regression of tumors. J Immunother Cancer. 2021;9(4).
48. Yang L, Zha TQ, He X, Chen L, Zhu Q, Wu WB, et al. Placenta-specific protein 1 promotes cell proliferation and invasion in non-small cell lung cancer. Oncology reports. 2018;39(1):53–60.
49. Han S, Wang T, Chen Y, Han Z, Guo L, Wu Z, et al. High CCL7 expression is associated with migration, invasion and bone metastasis of non-small cell lung cancer cells. American journal of translational research. 2019;11(1):442–52.
50. Li N, Zeng Y, Tai M, Lin B, Zhu D, Luo Y, et al. Analysis of the Prognostic Value and Gene Expression Mechanism of SHOX2 in Lung Adenocarcinoma. Frontiers in molecular biosciences. 2021;8:688274.
51. Lin Y, Xu J, Lan H. Tumor-associated macrophages in tumor metastasis: biological roles and clinical therapeutic applications. Journal of hematology & oncology. 2019;12(1):76.
52. Ji J, Wang P, Zhou Q, Zhu L, Zhang H, Zhang Y, et al. CCL8 enhances sensitivity of cutaneous squamous cell carcinoma to photodynamic therapy by recruiting M1 macrophages. Photodiagnosis and photodynamic therapy. 2019;26:235–43.
53. Zhang X, Chen L, Dang WQ, Cao MF, Xiao JF, Lv SQ, et al. CCL8 secreted by tumor-associated macrophages promotes invasion and stemness of glioblastoma cells via ERK1/2 signaling. Laboratory investigation; a journal of technical methods and pathology. 2020;100(4):619–29.
54. Grande F, Giancotti G, Ioele G, Occhiuzzi MA, Garofalo A. An update on small molecules targeting CXCR4 as starting points for the development of anti-cancer therapeutics. European journal of medicinal chemistry. 2017;139:519–30.
55. Eckert F, Schilbach K, Klumpp L, Bardoscia L, Sezgin EC, Schwab M, et al. Potential Role of CXCR4 Targeting in the Context of Radiotherapy and Immunotherapy of Cancer. Frontiers in immunology. 2018;9:3018.
56. Wald O. CXCR4 Based Therapeutics for Non-Small Cell Lung Cancer (NSCLC). Journal of clinical medicine. 2018;7(10).
57. Lutz ER, Wu AA, Bigelow E, Sharma R, Mo G, Soares K, et al. Immunotherapy converts nonimmunogenic pancreatic tumors into immunogenic foci of immune regulation. Cancer Immunol Res. 2014;2(7):616–31.

58. Kleponis J, Skelton R, Zheng L. Fueling the engine and releasing the break: combinational therapy of cancer vaccines and immune checkpoint inhibitors. Cancer biology & medicine. 2015;12(3):201–8.
59. Kang FB, Chen W, Wang L, Zhang YZ. The diverse functions of Siglec-15 in bone remodeling and antitumor responses. Pharmacological research. 2020;155:104728.
60. Murugesan G, Correia VG, Palma AS, Chai W, Li C, Feizi T, et al. Siglec-15 recognition of sialoglycans on tumor cell lines can occur independently of sialyl Tn antigen expression. Glycobiology. 2021;31(1):44–54.

Tables

Table 1. Designed sequences of the peptides of extracellular domain of S15 (A1-A12, B1-B11)

Detailed sequences of the peptides of extracellular domain of S15			
A1	HSSPAQRWSMQV	B1	RWSMQVPPEVSA
A2	PPEVSAEAGDAA	B2	EAGDAAVLPCTF
A3	VLPCTFTHPHRH	B3	THPHRHYDGPLT
A4	YDGPLTAIWRAG	B4	AIWRAGEPYAGP
A5	EPYAGPQVFRCA	B5	QVFRCAAARGSE
A6	AARGSELCQTAL	B6	LCQTALSLHGRF
A7	SLHGRFRLLGNP	B7	RLLGNPRRNDLS
A8	RRNDLSLRVERL	B8	LRVERLALADDR
A9	ALADDRRYFCRV	B9	RYFCRVEFAGDV
A10	EFAGDVHDRYES	B10	HDRYESRHGVRL
A11	RHGVRLHVTAAP	B11	HVTAAPRIVNIS
A12	RIVNISVLPSPA		

S15: Siglec-15

Figures

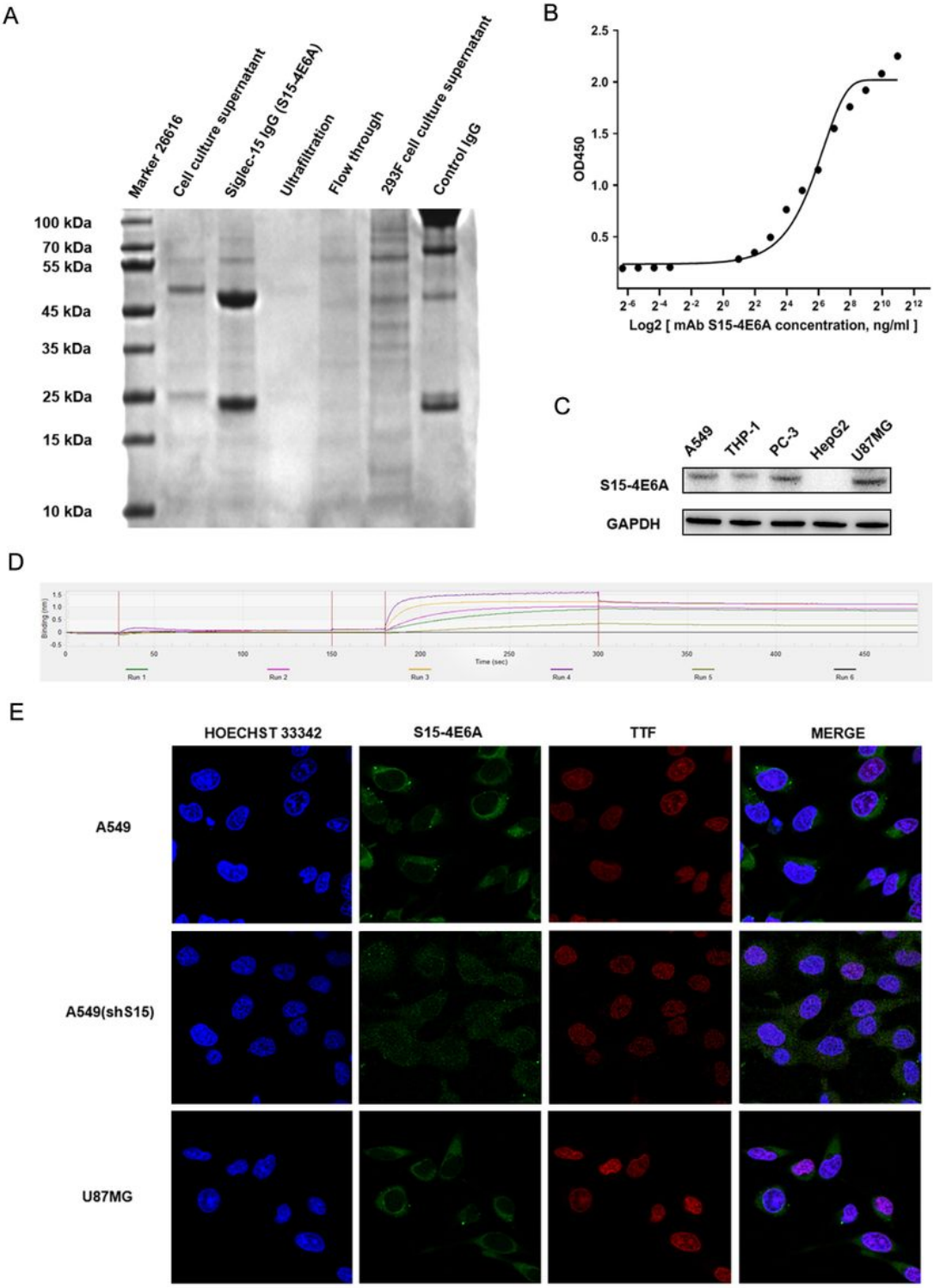

Figure 1

A. SDS-PAGE was performed to validate the successful construction of S15-4E6A. The red arrow indicates the heavy chain of S15-4E6A, while blue represents the light chain of S15-4E6A. B. ELISA analysis demonstrated the significant binding of S15-4E6A to the S15 protein in a dose-dependent manner. C. WB showed that S15-4E6A could react with S15-positive cell lines including the U87MG, PC-3, THP-1, and A549 cell lines but failed to recognize the S15-negative cell line HepG2. D. A BLITz affinity

assay suggested that the equilibrium dissociation constant (Kd) for S15-4E6A was 5.719×10^{-8} M. D. IF analysis illustrated that S15 could be stained by S15-4E6A in the A549 (S15-positive) cell line. As S15 was downregulated, the staining intensity of S15-4E6A decreased significantly. Positive staining of S15 was dominantly localized in the cytomembrane, while relatively weak staining of S15 was detected in the cytoplasm of cancer cells. The U87MG cell line was employed as a positive control. HOECHST33342 is a blue light-emitting fluorescent compound widely used for nuclear staining. TTF was also employed as a red light-emitting nuclear stain. Green staining represents the S15 protein recognized by S15-4E6A.

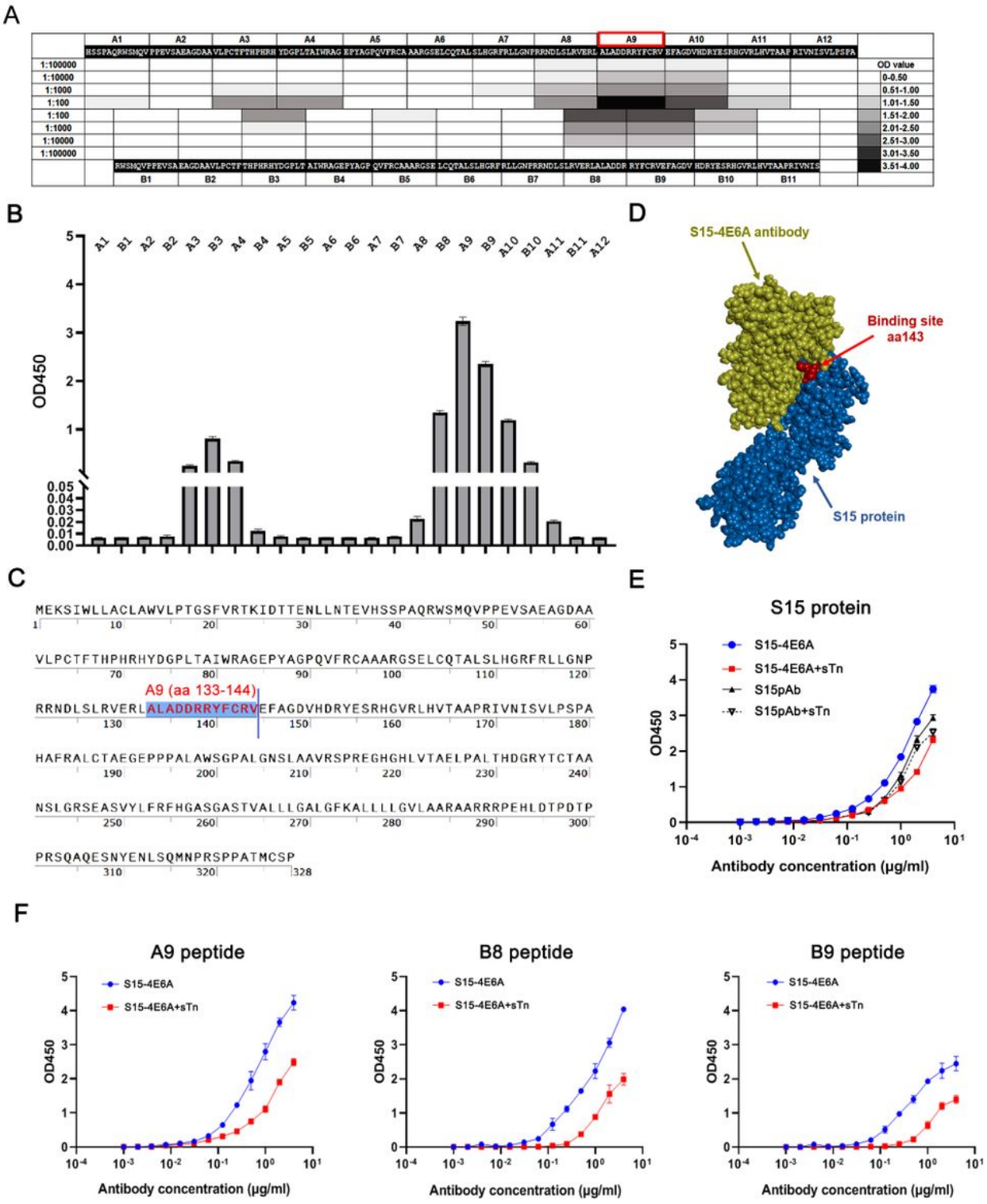

Figure 2

A and B. The extracellular domain of S15 (aa 37–180) was used as a template and deliberately divided into 23 segments, A1-A12 and B1-B11, in which the B serial sequences could completely cover the A serial sequences. An epitope mapping test showed that the OD value of the A9 segment was the highest among the segment OD values when the polypeptide dilution ratio was 1:100. C. The detailed amino acid of the A9 sequence was ALADDRRYFCRV (aa 133–144). D. Discovery Studio 2019 software (Dassault Systèmes Biovia, CA, USA) was employed to create a 3D diagram of the recognition of S15 by S15-4E6A. Specifically, the S15 protein sequence was input, homology modeling was adopted, and the template with the highest score was selected. Then, the sequence of the anti-S15 antibody was input, and the antibody modeling program was applied. The ZDOCK program was utilized to dock the abovementioned S15 protein and anti-S15 antibody, and the RDOCK program was conducted to optimize the docking procedure. Finally, the simulation model was operated to analyze the molecular interaction, and the charmm force field was implemented to calculate the binding force. The value of the molecular interaction was -126.03084 kcal/mol. E. A competitive inhibition test demonstrated that S15-4E6A could increasingly bind to S15 in a dose-dependent manner while progressively weakening the binding of sTn to S15. F. In comparison, the A9 sequence demonstrated the most significant binding ability for S15-4E6A among the three sequences containing epitope sites (A9, B8 and B9).

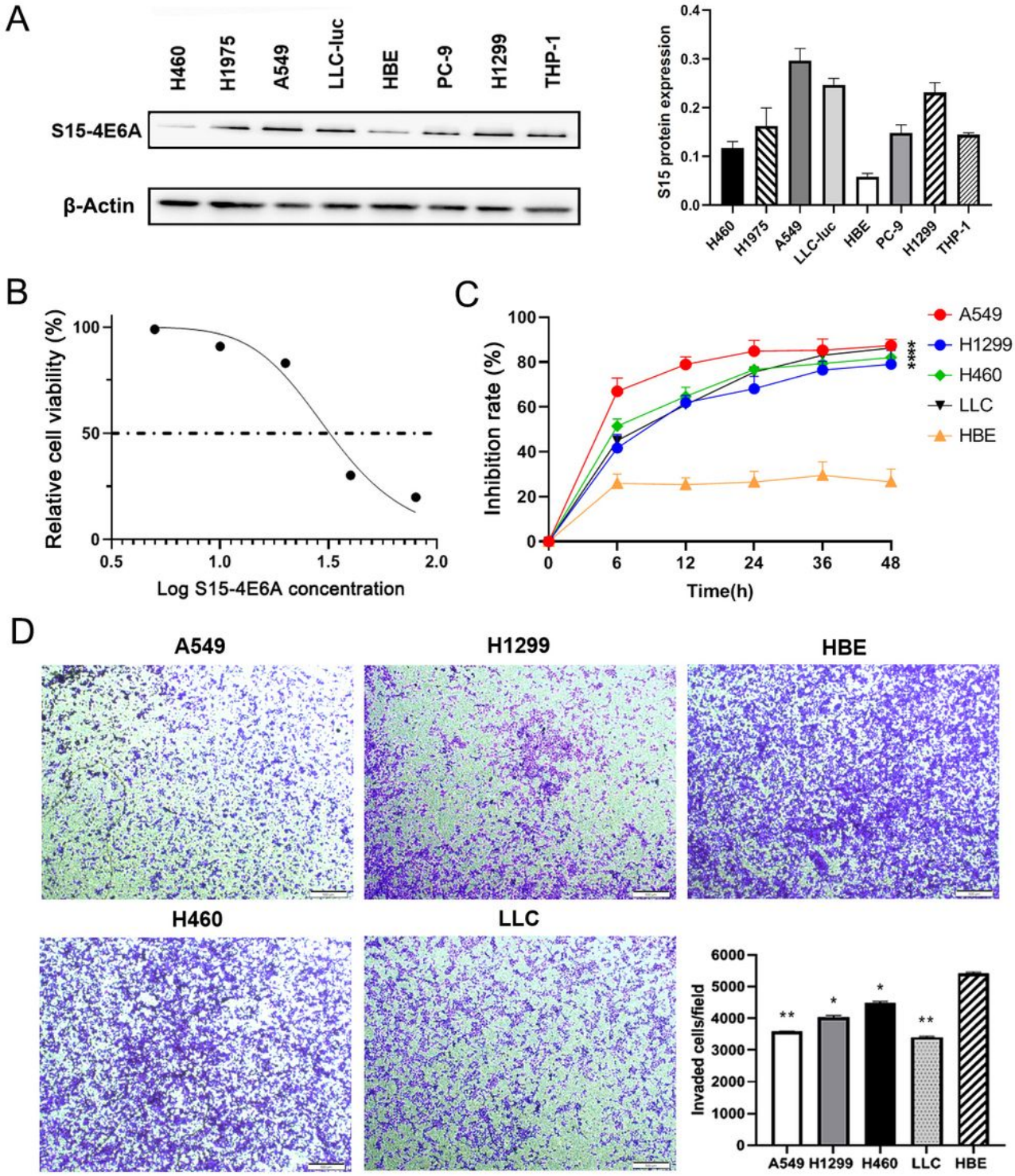

Figure 3

A. S15 expression in several human lung cancer cell lines and one luciferase-labeled mouse LUAD cell line (LLC-luc) was detected by WB. B. A dose-effect curve was generated to determine the IC50 (1.505) of S15-4E6A in A549 cells. An appropriate concentration of S15-4E6A (20 μg/mL) was selected for subsequent experiments. C. A CCK-8 assay showed that the inhibition efficiency of S15-4E6A was significantly increased in a time-dependent manner in S15-positive cell lines (A549, H1299, H460, LLC)

but not in an S15-negative cell line (HBE). *Significant difference of inhibition rate in LUAD cell lines compared with HBE cell line. *p < 0.05. D. Transwell analysis revealed that the number of invasive cells with high S15 expression was significantly lower than that of cells with low S15 expression after treatment with S15-4E6A. *Significant difference of invasive cells in LUAD cell lines compared with HBE cell line. *p < 0.05, **p < 0.01.

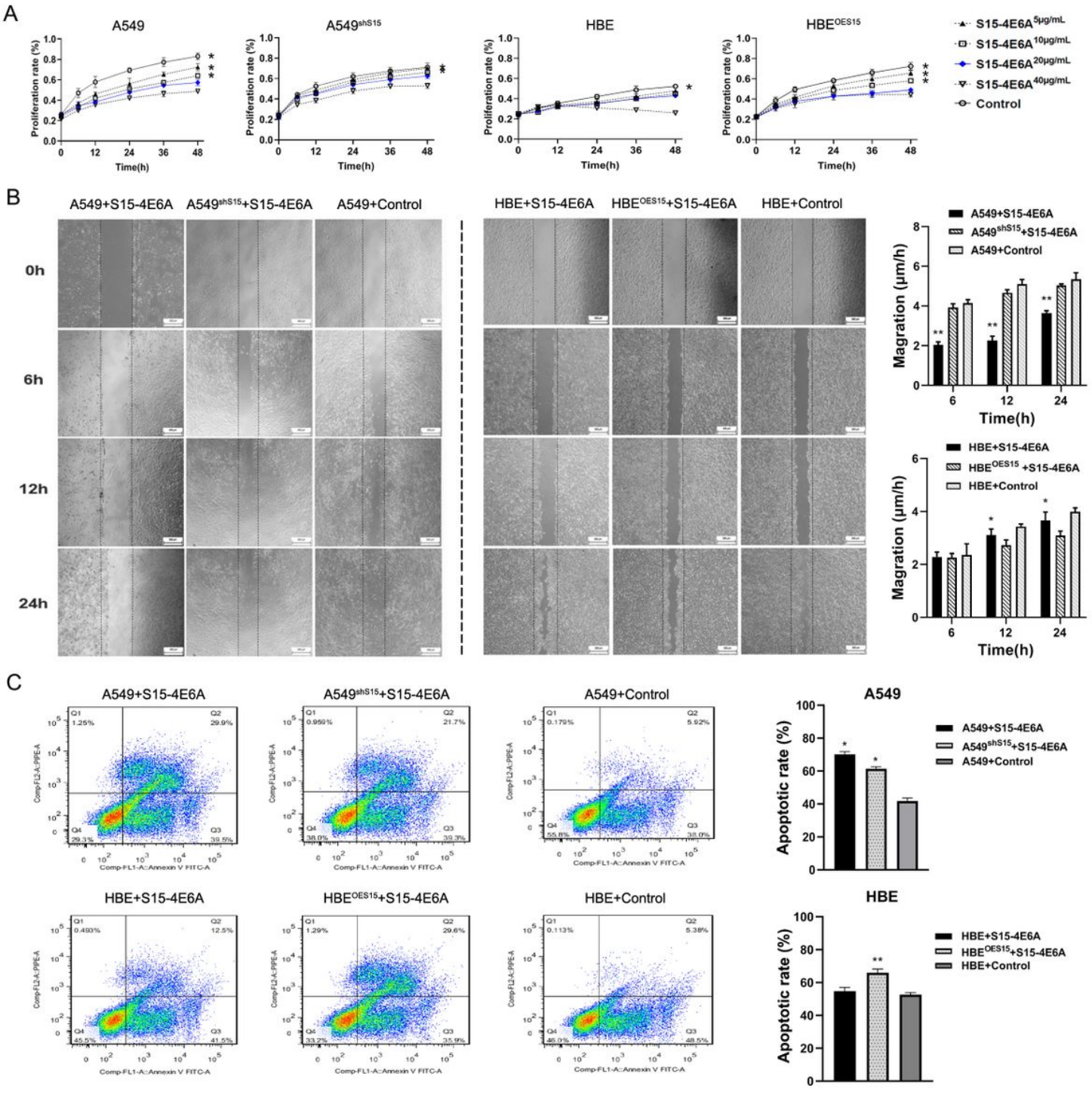

Figure 4

A. A CCK-8 assay demonstrated that cell proliferation was dramatically increased when S15 expression was knocked down in the A549 cell line (A549shS15) after S15-4E6A administration. In comparison, cell proliferation was critically inhibited when S15 was overexpressed in an HBE cell line (HBEOES15). *Significant difference of proliferation rate in in S15-4E6A treatment group compared with control group. *$p < 0.05$. B. A wound healing assay showed that cell migration was significantly increased when S15 expression was knocked down in the A549 cell line ($A549^{shS15}$) after S15-4E6A administration. In comparison, cell proliferation was tremendously inhibited when S15 was overexpressed in the HBE cell line (HBE^{OES15}). *Significant difference of migration rate in A549 and HBE cell lines in S15-4E6A treatment group compared with that of in control group. *$p < 0.05$, **$p < 0.01$. C. An Annexin V/PI assay revealed that the apoptotic rate was remarkably decreased when S15 expression was knocked down in the A549 cell line ($A549^{shS15}$) after S15-4E6A administration. In comparison, cell apoptosis was significantly elevated when S15 was overexpressed in the HBE cell line (HBE^{OES15}). *Significant difference of apoptotic rate in A549 and HBE cell lines in S15-4E6A treatment group compared with that of in control group. *$p < 0.05$, **$p < 0.01$.

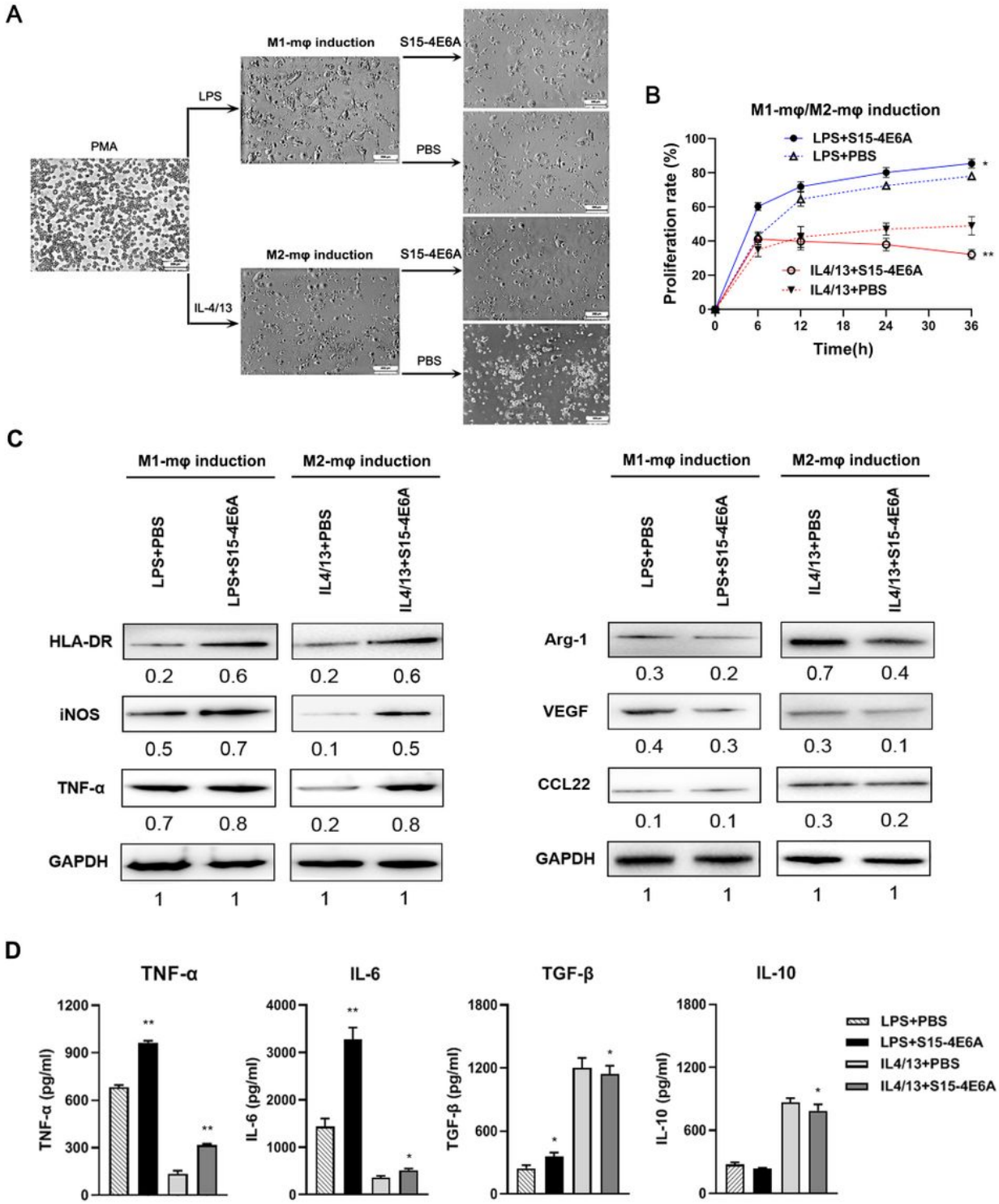

Figure 5

A. PMA was first employed to induce mφs, and LPS and IL-4/IL13 were used for M1 and M2-mφ polarization, respectively. Then, S15-4E6A was administered to both groups, and PBS was used as a negative control. B. S15-4E6A dramatically accelerated the cell proliferation rate in the M1-mφ group (LPS induction) but reduced the cell proliferation rate in the M2-mφ group (IL4/13 induction). *Significant difference of proliferation in S15-4E6A treatment group compared with that of in PBS group. *p < 0.05,

**p < 0.01. C. WB showed that an M1-mφ marker (iNOS) and related genes (HLA-DR and TNF-α) were upregulated, while an M2-mφ marker (Arg-1) and related genes (VEGF, CCL22) were downregulated after S15-4E6A administration in both the M1 and M2-mφ induction groups. D. ELISA showed that TNF-α and IL-6 expression was elevated, while TGF-β and IL-10 expression was downregulated after S15-4E6A was used to treat both the M1-mφ and M2-mφ groups. *Significant difference of cytokine expression in S15-4E6A treatment group compared with that of in PBS group. *p < 0.05, **p < 0.01.

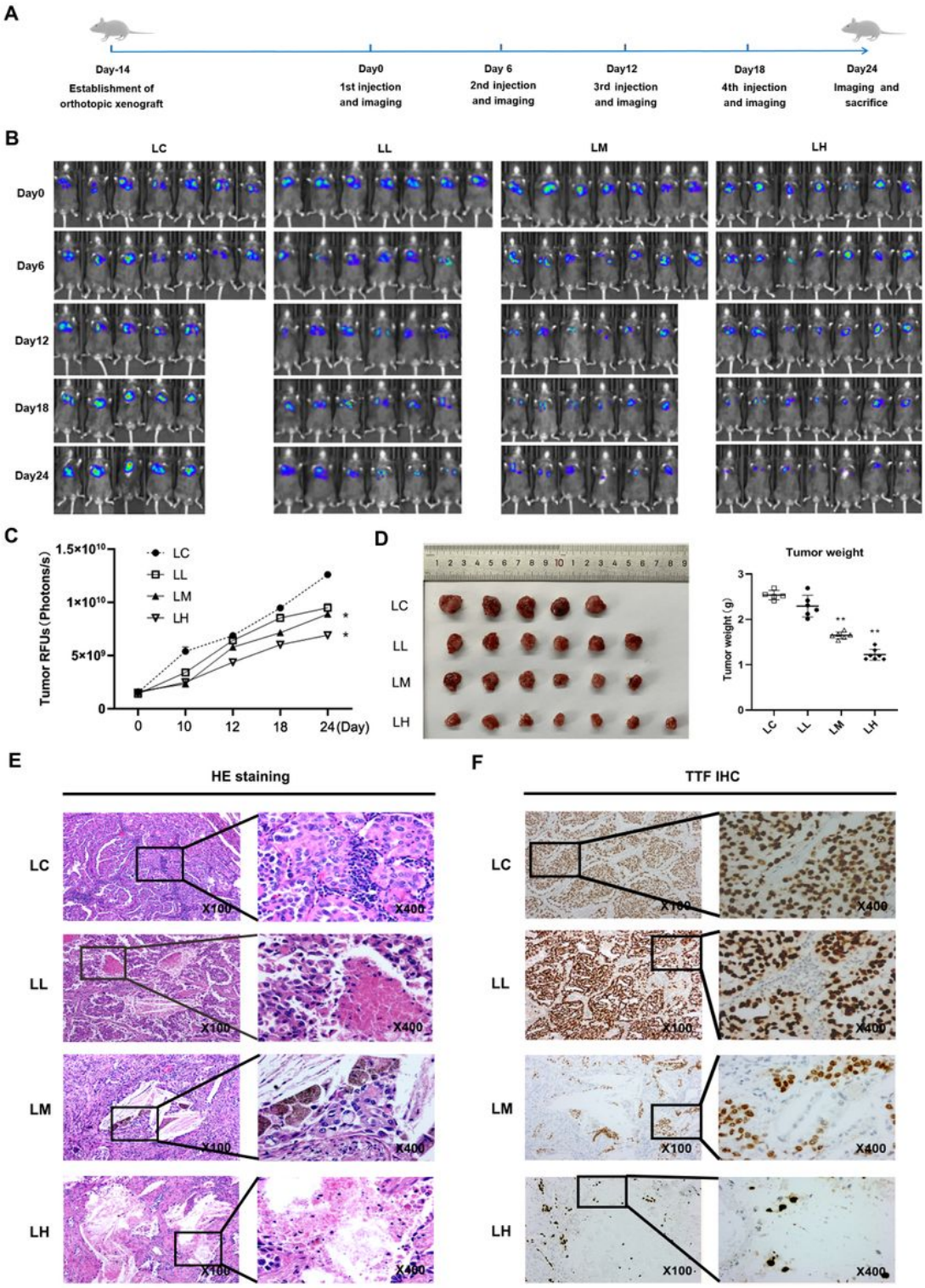

Figure 6

A flow diagram of LUAD orthotopic xenograft tumor model construction and S15-4E6A administration. Mice were orthotopically implanted with luciferase-expressing cells (LLC-LUC cells) and then randomly divided into four groups (LC, LL, LM, and LH). On days 0, 6, 12 and 18, the mice received intravenous treatment with S15-4E6A at various concentrations (1 mg/kg - 10 mg/kg). B and C. Serial bioluminescence images and tumor signals in mice were recorded. Bioluminescence imaging of xenograft LUAD tumors derived from luciferase-expressing LLC-LUC cells demonstrated a dramatic inhibitory effect on tumors by S15-4E6A, and the LH group exhibited the most significant tumor-inhibitory effectiveness.*Significant difference in tumor RFUs in S15-4E6A treatment group (LH and LM) compared with that of in control group (LC). *$p < 0.05$. D. Comparison of xenograft morphology and tumor weight among different S15-4E6A treatment groups. *Significant difference in tumor weight in S15-4E6A treatment group (LH and LM) compared with that of in control group (LC). **$p < 0.01$. E. H&E staining confirmed that a small amount of chronic inflammatory cell infiltration was observed in the stroma of tumors (LC group). In comparison, necrotic areas and interstitial fibrosis were observed after high-dose S15-4E6A administration (LH group). F. IHC analysis proved that as the S15-4E6A concentration increased, TTF expression gradually decreased.

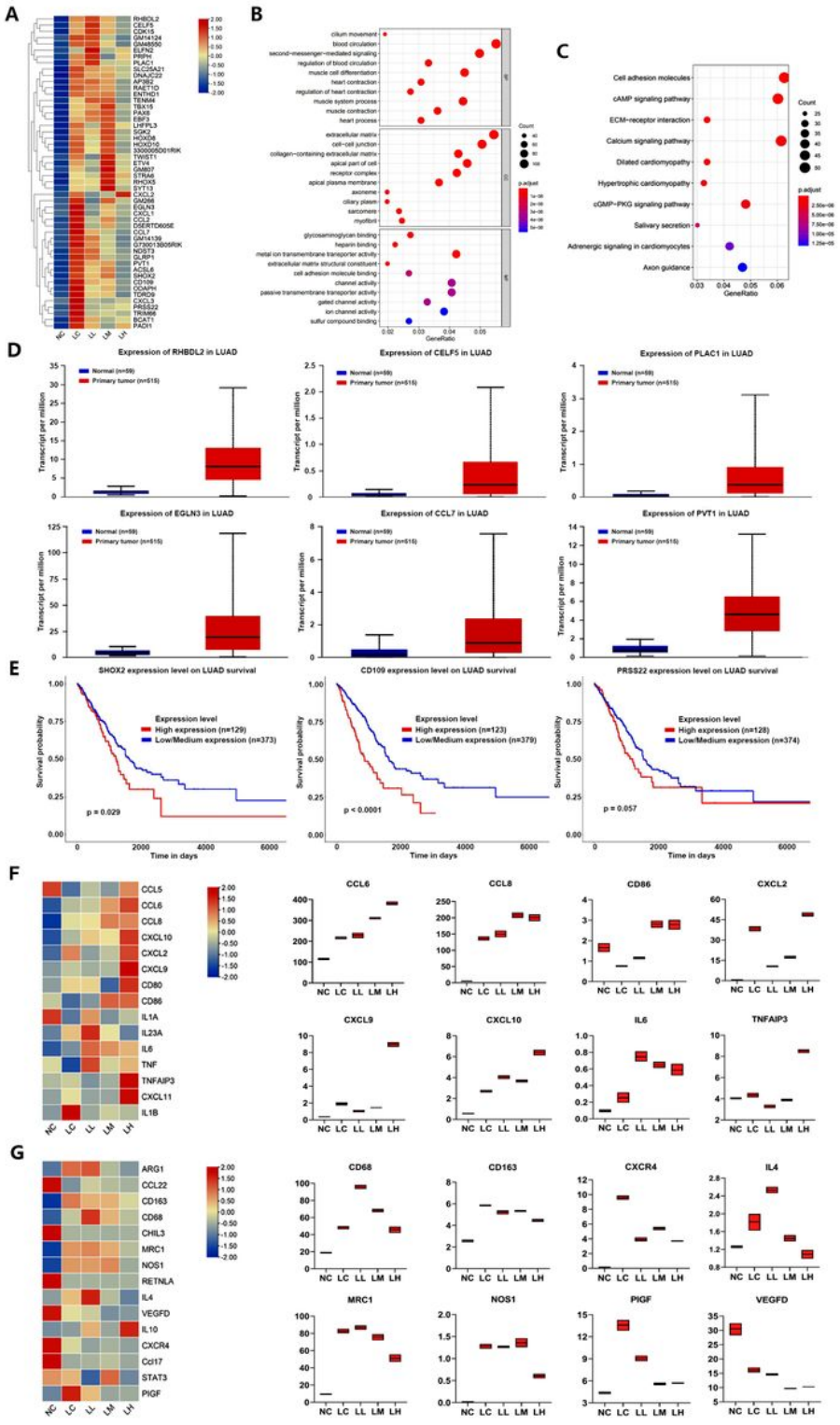

Figure 7

A. Heatmap of the top 50 most significantly upregulated genes with various S15-4E6A treatments. B. GO analysis showed that upregulated genes were largely associated with terms including second-messenger-mediated signaling, cell-cell junction, receptor complex, cell adhesion molecule binding and so on. C. KEGG enrichment results showed that DEGs were significantly enriched in cell adhesion molecules, the cAMP signaling pathway, ECM-receptor interaction, and cGMP-PKG signaling pathways. D. The TCGA

data for LUAD was consulted, and six elevated genes including RHBDL2, CELF5, PLAC1, EGLN3, CCL7, and PVT1 were screened. E. High expression of SHOX2, CD109, and PRSS22 indicated a poor prognosis for LUAD patients. F and G. Heatmap of mφ-related DEGs in different S15-4E6A treatment groups. M1 mφ-associated genes included CCL6, CCL8, CD86, CXCL2, CXCL9, CXCL10, IL6, and TNFAIP3. M2 mφ-associated genes included CD68, CD163, CXCR4, IL4, MRC1, NOS1, PIGF, and VEGFD.

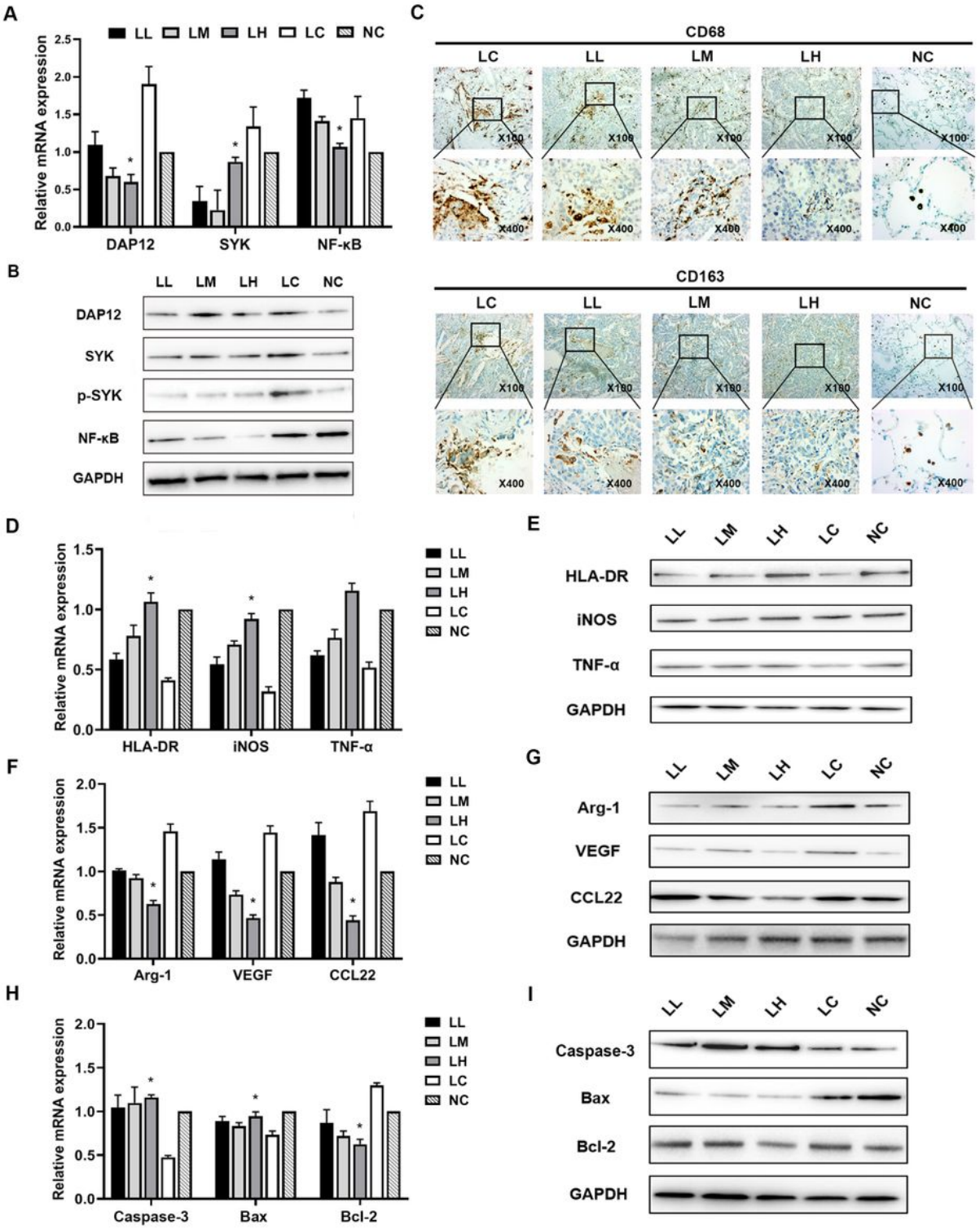

Figure 8

A and B. The qPCR and WB results identified that S15-4E6A treatment significantly suspended the expression of DAP12-SYK-NF-κB signaling pathway. *Significant difference of DAP12, SYK and NF-κB expression in S15-4E6A treatment group (LH) compared with that of in control group (LC). *p < 0.05. C. IHC analysis proved that the expression of CD68 and CD163 was dramatically downregulated in the LH S15-4E6A group. D and E. qPCR and WB demonstrated that M1-mφ-related markers (iNOS, HLA-DR, and TNF-α) were significantly upregulated after S15-4E6A administration in mice. *Significant difference of iNOS, HLA-DR and TNF-α expression in S15-4E6A treatment group (LH) compared with that of in control group (LC). *p < 0.05. F and G. M2 mφ-related markers (Arg-1, VEGF, and CCL22) were dramatically downregulated after S15-4E6A administration in mice. *Significant difference of Arg-1, VEGF and CCL22 expression in S15-4E6A treatment group (LH) compared with that of in control group (LC). *p < 0.05. H and I. FCM analysis revealed that the antiapoptotic factor Bcl-2 was significantly downregulated, while the proapoptotic factors Bax and caspase-3 were dramatically upregulated in the LH S15-4E6A group compared with the control group. *Significant difference of Caspase-3, Bax and Bcl-2 expression in S15-4E6A treatment group (LH) compared with that of in control group (LC). *p < 0.05.

Supplementary Files

This is a list of supplementary files associated with this preprint. Click to download.

- figureS1.jpg
- figureS2.jpg
- figureS3.jpg
- figureS4.jpg
- tableS1.docx
- tableS2.docx
- tableS3.docx